JACS Au
AN OPEN ACCESS JOURNAL OF THE AMERICAN CHEMICAL SOCIETY

pubs.acs.org/jacsau
Article

Palladium-Catalyzed Functionalization of Shortwave Infrared Heptamethine Fluorophores Expands Their In Vivo Utility

Cesar A. Garcia, Emily B. Mobley, Eric Y. Lin, Kyle Bui, and Ellen M. Sletten*

Cite This: JACS Au 2025, 5, 2089−2101
Read Online

ACCESS | Metrics & More | Article Recommendations | Supporting Information

ABSTRACT: Fluorescence imaging in the near-infrared (NIR, 700−1000 nm) and shortwave infrared (SWIR, 1000−2000 nm) regions is advantageous for studying mammals. This work applies palladium-catalyzed coupling methods to functionalize flavylium and chromenylium SWIR polymethine fluorophores, which are challenging substrates due to their small HOMO−LUMO gaps. These chemistries include Suzuki-Miyaura and Sonogashira couplings as well as an unprecedented coupling of alcohol substrates to ultimately achieve a panel of C−C_{Ar}, C−C_{sp}, and C−O-alkyl functionalized SWIR fluorescent heptamethine dyes. The photophysical properties of the resulting fluorophores are analyzed against Hammett parameters to produce predictive metrics for absorption maxima. These metrics are strategically applied in the design of laser-matched, SWIR-emissive, chromenylium heptamethine dyes. Added functionalities advance the utility of SWIR fluorophores by increasing brightness in micelle formulations, modulating lipophilicity for alternative delivery vehicles, and enabling bioconjugation to targeting moieties. Ultimately, three functionalized fluorophores are employed in concert to achieve multicolor excitation-multiplexed imaging in murine cancer models.

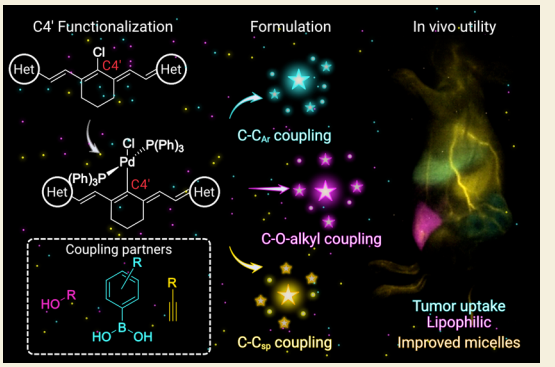

KEYWORDS: *multiplexed imaging, polymethine dyes, bioconjugation, cross-coupling, near-infrared, shortwave infrared*

INTRODUCTION

Fluorescence imaging in the near-infrared (NIR, 700−1000 nm) region of the electromagnetic spectrum is a classic approach to study mammals due to the enhanced penetration of NIR photons through tissue and decreased autofluorescence compared to visible (400−700 nm) wavelengths of light.[1−4] Heptamethine dyes, including the U.S. Food and Drug Administration (FDA) approved indocyanine green (ICG) and OTL-38, are common contrast agents employed for imaging in the NIR region.[5,6] This class of dyes is composed of two heterocycles connected by a conjugated heptamethine chain (Figure 1A). In many instances, the heptamethine linker contains a central cyclohexenyl moiety with a chlorine atom at the C4′ position that can be leveraged to introduce new functionalities to the fluorophore.[7−11] While the photophysical characteristics (e.g., absorbance maxima, quantum yield, absorption coefficient, brightness) of heptamethine dyes are often dictated by the heterocycle and/or polymethine chain length/rigidification, the C4′ position provides an additional site for altering functionality and fine-tuning the photophysical properties of the fluorophore.[12] Modification at the C4′ position enables the attachment of a new functional group while maintaining heterocycle symmetry, minimizing synthetic steps and maximizing photophysical properties. Hence, this position has been exploited to expand the utility of existing indolinium polymethine NIR fluorophores via attachment of: vitamins, for image assisted resection of ovarian cancer (e.g., OTL-38); antibodies, for targeted imaging; and small molecule therapeutics (see Chart S1 for examples of C4′ position functionalized cyanine heptamethine dyes).[5,13−18] Of the various linkages successfully appended at the C4′ position, carbon-aryl (C−C_{Ar}), carbon-alkyne (C−C_{sp}), and carbon−oxygen alkyl (C−O-alkyl) are preferred over C−R (R = NHAr, OAr, SAr) due to the improved resistance to nucleophilic attack in biologically relevant environments.[15−18]

While the C4′ position is often preferred for functionalization, the photophysical consequences of different transformations are not often considered. Ideally, the transformations imparted at the C4′ position are carefully selected to install the desired functionality through a biologically stable linkage, while also capitalizing on the resulting photophysical changes to maximize brightness. Although there has been great success in expanding the applications of NIR heptamethine dyes, limitations in depth penetration and background signal are still apparent in this detection window. The shortwave

Received: December 30, 2024
Revised: March 7, 2025
Accepted: March 10, 2025
Published: April 4, 2025

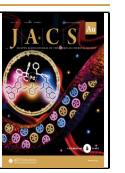

https://doi.org/10.1021/jacsau.4c01279
JACS Au 2025, 5, 2089−2101

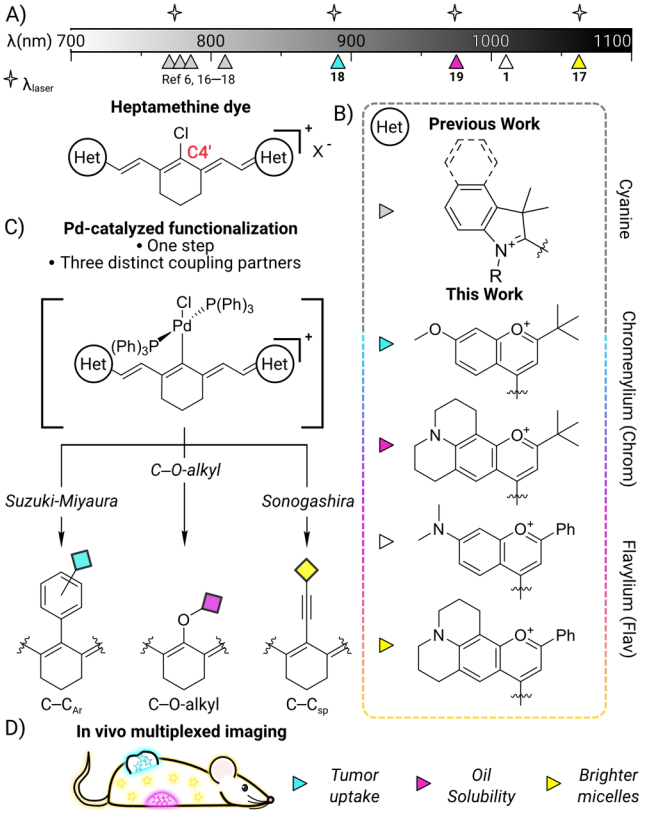

Figure 1. Heptamethine fluorophores functionalized at the C4′ position improve biological utility. A) General structure of heptamethine dyes and absorption maxima of dyes in (B). B) Structures of indolinium, chromenylium, and flavylium heterocycles. C) Palladium-catalyzed functionalization of SWIR heptamethine dyes. D) Application of C4′ position coupling chemistries for in vivo multiplexed imaging.

infrared (SWIR, 1000−2000 nm) has garnered interest toward in vivo imaging due to enhanced penetration of low energy light through tissue, lower autofluorescence of endogenous chromophores and decreased scattering resulting in higher signal-to-noise ratios compared to the NIR region.[19−22] Additionally, SWIR imaging allows for enhanced multiplexed imaging as there are more opportunities for imaging at separate wavelengths through either excitation or emission differentiation.[23]

SWIR-emissive heptamethine dyes can be accessed by exchanging traditional indolinium heterocycles for chromenylium heterocycles (Figure 1B). Chromenylium dyes and flavylium dyes (a subset of the chromenylium scaffold) have enabled cutting-edge noninvasive imaging in mice including four-color video-rate imaging and awake animal imaging.[23,24] These advances employed unfunctionalized heptamethine dyes delivered in micelle formulations. Unfortunately, the small HOMO−LUMO gap inherent to SWIR fluorophores leads to many pathways of side reactivity, complicating the use of functionalization strategies established for NIR fluorophores.[25−27] Thus, common functionalization methods, including S_NAr chemistry and aryl lithiate addition, have primarily been applied to NIR dyes.[7−14,28,29] Classic S_NAr methods typically introduce a biologically labile bond at the C4′ position (e.g., −NArH, −OAr, −SAr), while the recently reported aryl lithiate addition by Jia and co-workers produces stable $C−C_{Ph}$ bonds but requires a two-step sequence.[29]

Here, we explored the potential of the C4′ position as a functional handle for SWIR fluorophores utilizing palladium (Pd)-catalyzed chemistries. We employ cross-coupling methodologies to functionalize existing SWIR heptamethine scaffolds **Flav7**, **JuloChrom7**, and **JuloFlav7**, as well as a newly developed chromenylium fluorophore, **OMeChrom7**. The chemistry developed enabled cross-coupling of chromenylium heptamethine dyes at the C4′ position with Suzuki-Miyaura and Sonogashira coupling partners, paralleling successful transformations with NIR heptamethine dyes. Furthermore, we report installation of C−O-alkyl functionalities at the C4′ position through a palladium-catalyzed coupling of primary alcohols−a transformation not only unprecedented in both NIR and SWIR fluorophores, but also particularly challenging in unactivated, electron rich, aromatic systems (Figure 1C).[30] The structure−property relationships of the functionalized fluorophores are investigated, relating absorption maximum ($\lambda_{max,abs}$) with the type of chemical transformation, and predictive metrics are established. The trends observed are utilized to guide fluorophore design, maximizing brightness by fine-tuning $\lambda_{max,abs}$ to match three common commercial laser lines for biological imaging. Ultimately, these functionalization strategies are strategically applied to chromenylium and flavylium polymethine dyes to address solubility and/or bioaccumulation properties of SWIR-emissive heptamethine dyes, achieving three-color excitation-multiplexed imaging in murine cancer models (Figure 1D).

RESULTS AND DISCUSSION

Scope of Palladium$^{0/II}$-Catalyzed Chemistries

For method development, we focused on the modification of SWIR heptamethine dye, **Flav7** (**1**). First, we explored Suzuki-Miyaura coupling to modify the C4′ position, which was previously successful for modifying NIR heptamethine dyes.[30] Initial reaction conditions to couple **1** with phenyl boronic acid to form **1a** employed $Pd(PPh_3)_4$ and K_3PO_4. While dimethylformamide (DMF) readily solubilized all substrates, **1** rapidly decomposed at 60 °C within 2 h and no coupling was observed. To avoid degradation, a 5:1 1,4-dioxane:H_2O system was employed and >90% conversion to **1a** was achieved in 24 h at 90 °C, as calculated by liquid chromatography mass spectrometry (LCMS) (Figure S1). Encouraged by this result, we screened inexpensive commercial catalysts ($Pd(dba)_2$ and $Pd(OAc)_2$) and electron rich ligands (X-Phos and Ruphos) commonly available in the laboratory, but conversion was not enhanced. The final optimized conditions were established as $Pd(PPh_3)_4$, K_3PO_4 in a 5:1 1,4-dioxane:H_2O mixture at 90 °C which led to the coupling of phenyl boronic acid and **1** to produce **1a** in 60% isolated yield. The modest isolation yield is attributed to the affinity of **1a** to silica gel, a common challenge in the purification of chromenylium heptamethine dyes.[22]

With the optimized reaction conditions established, we sought to expand the scope of substrates coupled to **1** using aryl boronic acids containing functionalities that have been applied for bioconjugation and/or reducing nonemissive aggregation of polymethine dyes in biologically relevant media (i.e., aqueous environments).[31] We found that phenyl boronic acids containing azide, acid, or aldehyde functionalities could be installed (Scheme 1, **1b−e**). Additionally, boronic acids containing methyl or *tert*-butyl groups (**1f−g**) designed to sterically block chromophore aggregation were successfully coupled, although decreased conversion was observed, likely

https://doi.org/10.1021/jacsau.4c01279
JACS Au 2025, 5, 2089−2101

Scheme 1. Substrate Scope of Palladium-Catalyzed Coupling Chemistries

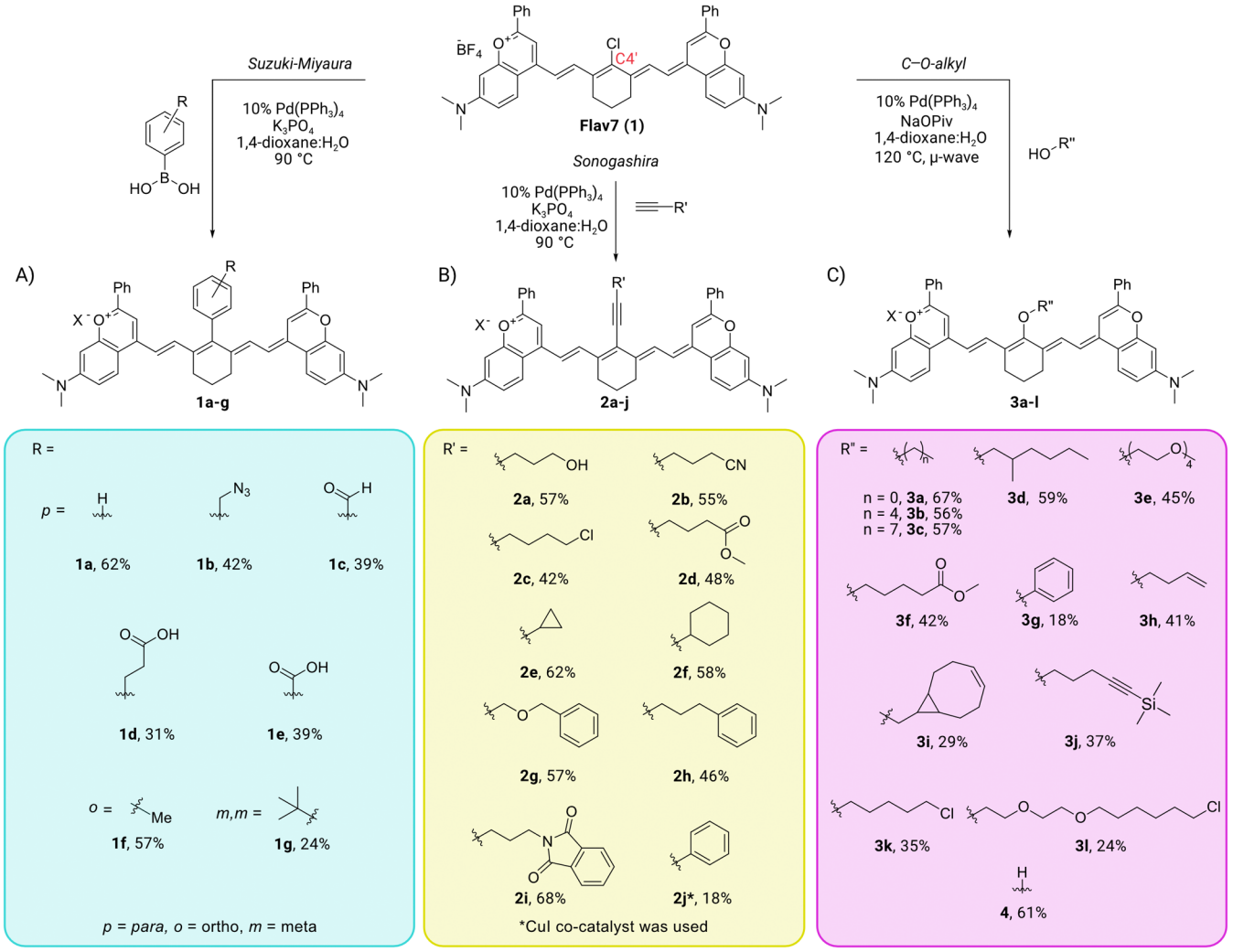

due to steric hindrance. From these initial couplings, we concluded that **1** was readily compatible with Pd-catalyzed chemistries.

Next, we sought to expand the scope of transformations applicable to the C4′ position through terminal alkyne coupling partners in a Sonogashira coupling reaction (Scheme 1B).[17] We first attempted to couple propargyl alcohol to **1** with analogous conditions to those of the Suzuki-Miyaura chemistry, but instead observed significant degradation. Employing a longer methylene spacer between the alkyne and alcohol resulted in successful coupling to form **2a** in 88% conversion, and 57% isolated yield (Figure S2). We found that substrates with alcohol, halogen, ester, cyano, phenyl, ether, or phthalimide (**2a–d, 2g–i**) functionality were well tolerated as long as a methylene spacer was used. The Sonogashira coupling was also amenable to alkyl substrates with increased steric bulk that did not require a methylene spacer (**2e–f**). When attempting to couple conjugated terminal alkynes (**2j**), decomposition was initially observed. However, the use of classic Sonogashira conditions with a Cu(I) cocatalyst resulted in successful coupling of phenylacetylene.

During the exploration of these transformations, we observed the transformation of **1** to product **3a** with $-OCH_2CH_3$ at the C4′ position when utilizing a 1,4-dioxane:EtOH mixture as the solvent (Figure S3). Etherification occurring at the C4′ position was a particularly exciting finding as methods to synthesize vinyl/aryl ethers with alcohols and unactivated vinyl/aryl halides typically require harsh conditions (e.g., Williamson ether synthesis, Ullmann reaction, Mitsunobu).[32−35] To circumvent this, previous methods to install stable C−O-alkyl modifications on NIR fluorophores have involved multistep rearrangements.[16,28]

To further explore the vinyl etherification, we optimized the coupling of **1** with pentanol to form **3b**, simplifying LCMS analysis (Figure S4). Our initial reaction conditions of $Pd(PPh_3)_4$ and K_3PO_4 in a 5:1 1,4-dioxane:H_2O mixture at 90 °C for 24 h proved fruitful with 40 equiv of the alcohol substrate. These conditions ultimately led to 81% conversion to the pentanol coupled substrate **3b** and 9% to byproduct **4**, the coupling of hydroxyl at the C4′ position. Compound was a minor product observed in Suzuki-Miyaura and Sonogashira couplings as well. Byproduct quickly tautomerizes to the C4′ position ketone, deemed bis-dipole fluorophore **4′**. We were able to increase the rate of conversion to **3b** using microwave irradiation at 120 °C for 20 min, ultimately providing 79% conversion to **3b** and 12% to byproduct **4** (Figure S5).

The novelty of the vinyl etherification prompted us to investigate its palladium dependency. Overall, the formation of vinyl alkyl ethers in polymethine dyes via direct S_NAr substitution at the C4′ position is scarcely reported due to

https://doi.org/10.1021/jacsau.4c01279
JACS Au 2025, 5, 2089−2101

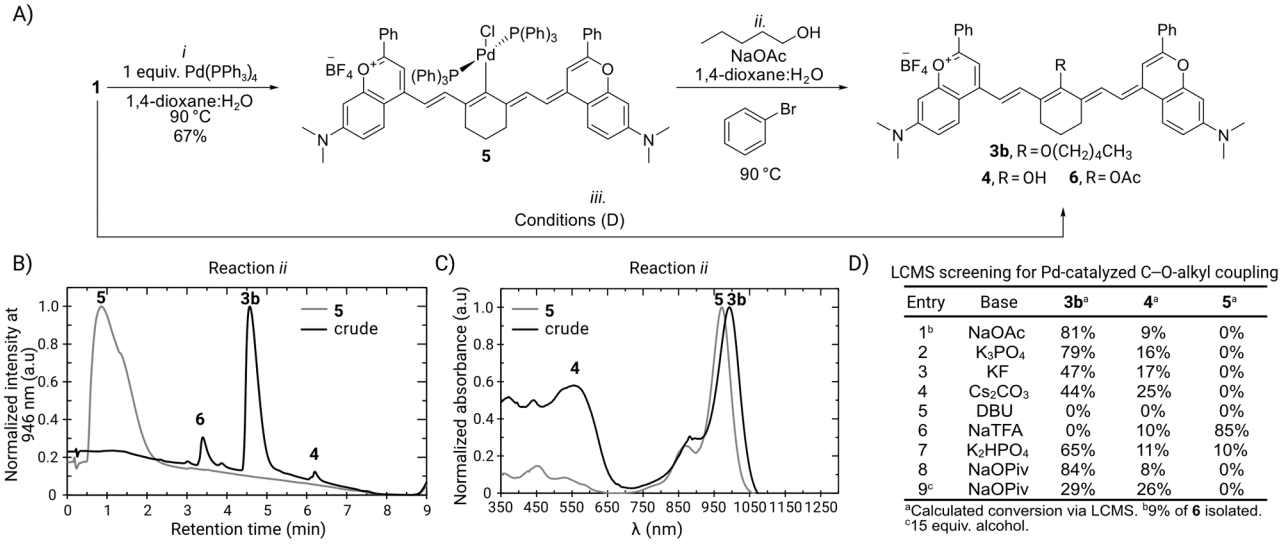

Entry	Base	3b[a]	4[a]	5[a]
1[b]	NaOAc	81%	9%	0%
2	K_3PO_4	79%	16%	0%
3	KF	47%	17%	0%
4	Cs_2CO_3	44%	25%	0%
5	DBU	0%	0%	0%
6	NaTFA	0%	10%	85%
7	K_2HPO_4	65%	11%	10%
8	NaOPiv	84%	8%	0%
9[c]	NaOPiv	29%	26%	0%

[a]Calculated conversion via LCMS. [b]9% of **6** isolated. [c]15 equiv. alcohol.

Figure 2. Palladium dependency of the C−O-alkyl transformation and condition screens. A) Conditions used to yield the oxidative addition complex (**5**) and subsequent alcohol coupling. B) LCMS data of **5** overlaid with the crude reaction mixture. C) Absorbance spectra (taken in DCM) showing the change in λ_{max} used to monitor product formation. D) Base screen. Conditions: *iii*. Base, $Pd(PPh_3)_4$, $CH_3(CH_2)_4OH$, 1,4-dioxane:H_2O, 120 °C (μ-wave), 20 min.

the poor kinetics of the alkoxide nucleophile, undesired regioselectivity, or lack of reactivity.[11,28] To rule out an S_NAr mechanism, the reaction was performed in the absence of metal catalyst or in the presence of ligand. LCMS analysis revealed no conversion to **3b** in either case, suggesting palladium dependency (Figure S6). We also observed that hydroxylated byproduct **4** was formed in a palladium- and water-dependent manner. Note that water is a required cosolvent for this transformation (Figure S6).

To further confirm palladium-catalysis as the mechanistic pathway, the oxidative addition (OA) complex **5** was isolated in the absence of a coupling partner. Palladium(II) complexes of cyanine polymethine dyes have been successfully isolated previously by Marder and co-workers under similar conditions.[36] Subjecting **5** to coupling conditions with bromobenzene as a Pd^0 trap led to the formation of product **3b**, as indicated by a red-shift in absorbance observed with UV-vis spectroscopy, and a shift in retention time and associated mass by LCMS analysis (Figure 2A−C). These results support the palladium dependency of this transformation. Furthermore, the stability of the OA complex and its potential to engage with thiols opens the door for future use as a stoichiometric bioconjugation reagent, as shown by Buchwald and co-workers.[37]

With the palladium dependency of this transformation established, we further optimized the etherification reaction with a focus on reducing the formation of **4**. While solvent and catalyst changes were not productive, we did observe significant differences when varying the base (Figure 2D). The use of inorganic bases favored conversion to **3b** (Entry 3, 4, 7), whereas the use of an amine base (Entry 5) completely degraded the fluorophore. Using weak bases (Entry 6), the OA complex was observed, indicating slow transmetalation of the alcohol substrate. Employing NaOAc resulted in higher conversion to product **3b** but also in the formation of the acetate addition at the C4′ position, **6**, a pathway we minimized by using the bulkier NaOPiv (Entry 8). Finally, lowering the alcohol equivalences dampened conversion (Entry 9), solidifying Entry 8 as the optimized conditions.

Next, we explored the scope of the C−O etherification reaction (Scheme 1C). Generally, alkyl alcohols (**3a−d**) coupled well with conversion rates between 65−85% and isolated yields of 54−67%. Methoxy-capped polyethylene glycol (PEG, **3e**), methyl ester (**3f**), and phenol (**3g**) were tolerated. Attempts to impart further functionality with a short chain alkene gave moderate yields (**3h**) while cyclic alkenes had lower yields (**3i**). In order to install alkyne functionality, we had to circumvent Sonogashira coupling from out-competing the C−O-alkyl transformation via a TMS-protected coupling partner. This substrate blocked Sonogashira coupling to afford the desired vinyl ether (**3j**). Finally, we successfully installed halogen-containing alcohols (**3k**) and protein labeling (i.e., HaloTag ligand) moieties (**3l**). Unfortunately, alcohols containing other bioconjugation handles such as azide or cyclooctyne were not able to be installed directly. The formation of C−O-alkyl bonds via palladium catalysis with primary alcohols is a current challenge in the field, requiring extensive ligand and catalyst design and optimization.[30] While the yields of this transformation are low with respect to the SWIR polymethine scaffold, it can be performed with a readily available commercial catalyst.

Taken together, these three palladium-catalyzed transformations have enabled a range of functionalities to be covalently appended to the C4′ position of **Flav7**. Common bioconjugation handles, protein labeling tags, and other reactive moieties (nitriles, alkenes, esters, and halogens) were successfully appended. Bulky substituents associated with decreased aggregation were also incorporated. With a general method for coupling three distinct coupling partners using the same readily accessible catalyst, we demonstrated a broad substrate scope and elected to omit screening of more specialized catalysts for further elaboration. These experiments demonstrate our ability to efficiently functionalize heptamethine flavylium dyes with a variety of functional groups, and report a new method to introduce C−O-alkyl functionality to heptamethine dyes.

https://doi.org/10.1021/jacsau.4c01279
JACS Au 2025, 5, 2089−2101

Scheme 2. Common Bioconjugation Approaches Applied to Functionalized Flav7 Derivatives[a]

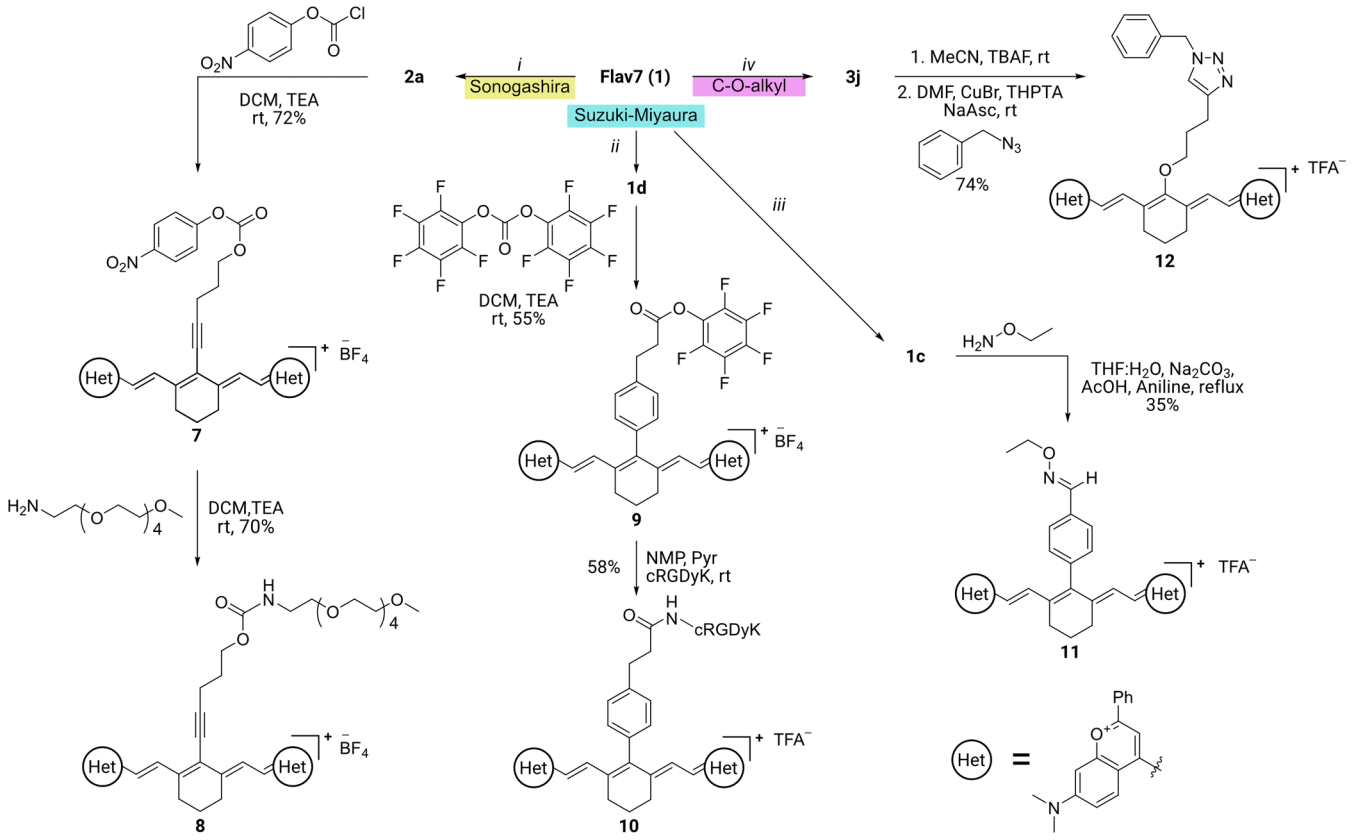

[a]Conditions: *i*. Pentynol, K_3PO_4, $Pd(PPh_3)_4$, 1,4-dioxane:H_2O, 90 °C. *ii*. 4-carboxyethyl phenyl boronic acid, K_3PO_4, $Pd(PPh_3)_4$, 1,4-dioxane:H_2O, 90 °C. *iii*. 4-formyl phenyl boronic acid, K_3PO_4, $Pd(PPh_3)_4$, 1,4-dioxane:H_2O, 90 °C. *iv*. trimethyl(pent-4-yn-1-yloxy)silane, NaOPiv, $Pd(PPh_3)_4$, 1,4-dioxane:H_2O, 120 °C (μ-wave), 20 min.

Further Derivatization of Flav7 Probes with Standard Bioconjugation Chemistries

Having established three palladium-catalyzed coupling chemistries for **Flav7** modification, we further elaborated these functional dyes with classic bioconjugation chemistries (Scheme 2). We initially pursued amide and carbamate formation via amine conjugation. For demonstration of carbamate formation, we began from Sonogashira product **2a** and activated with *p*-nitrophenyl chloroformate to yield **7**. Fluorophore **7** was then combined with 2,5,8,11-tetraoxatridecan-13-ol to create a carbonate linkage, **8**. We also forged an amide bond by activating acid-containing **1e** as a pentafluorophenyl (PFP) ester, **9**, which could then be combined with a variety of amines including the cyclic RGDyK (cRGD) peptide, an affinity peptide targeting $\alpha_v\beta_{III}$, receptors overexpressed in some cancer cells.[38] This strategy has been effectively applied to image $\alpha_v\beta_{III}$ expressing tumors in the NIR and SWIR regions.[39−43]

Next, we deprotected C−O-alkyl coupled product **3j** containing a TMS-acetylene such that it could undergo Cu(I)-catalyzed azide−alkyne cycloaddition (i.e., CuAAC, or "click chemistry"). The click chemistry reaction to yield **12**proceeded well, demonstrating that the flavylium dyes are compatible with one of the most popular approaches to (bio)conjugation. Capitalizing on another click-type reaction, aldehyde-containing **1c** readily condensed with *o*-ethylhydroxylamine to form stable oxime product **11**. With three cross-coupling methodologies and compatibility with standard conjugation chemistries established, we looked to optimize the flavylium fluorophores for bright, targeted, multicolor SWIR imaging.

Photophysical Characterization and Hammett Analysis of Functionalized Fluorophores

Before proceeding to in vivo imaging with modified flavylium dyes, we sought to understand the photophysical consequences of modification at the C4′ position. Heptamethine dyes are exceptional probes due to their high quantum yields of fluorescence (Φ_F), absorption coefficients (ε), and their narrow absorption/emission profiles. Selecting **8** ($\lambda_{max,abs}$ = 1031, $\lambda_{max,em}$ = 1057 nm, Φ_F = 0.62%), **11** ($\lambda_{max,abs}$ = 1007, $\lambda_{max,em}$ = 1029 nm, Φ_F = 0.53%), and **12** ($\lambda_{max,abs}$ = 997, $\lambda_{max,em}$ = 1021 nm, Φ_F = 0.62%) as representative of the diversity of chemistries applied, we see that the sharp absorption profile, narrow Stokes shift, and high Φ_F characteristic of **Flav7** in DCM are maintained (Figure 3A), suggesting these new C4′-modified dyes will be excellent candidates for in vivo imaging.

Looking more closely, changes in $\lambda_{max,abs}$ and $\lambda_{max,em}$ were observed for each of the three fluorophores. We hypothesized that these changes were due to the C4′ position modification being in conjugation with the chromophore. To this end, we investigated the change in absorbance of cross-coupled fluorophores **1a−g, 2a−j, 3a−l** in relation to **Flav7** by plotting $\Delta\lambda_{max,abs}$ for each functionalized derivative (Figure 3B). Our results indicate that Suzuki-Miyaura coupling leads to an average 20 ± 3 nm hypsochromic shift, while Sonogashira coupling imparts an average bathochromic shift of 6 ± 3 nm,

https://doi.org/10.1021/jacsau.4c01279
JACS Au 2025, 5, 2089−2101

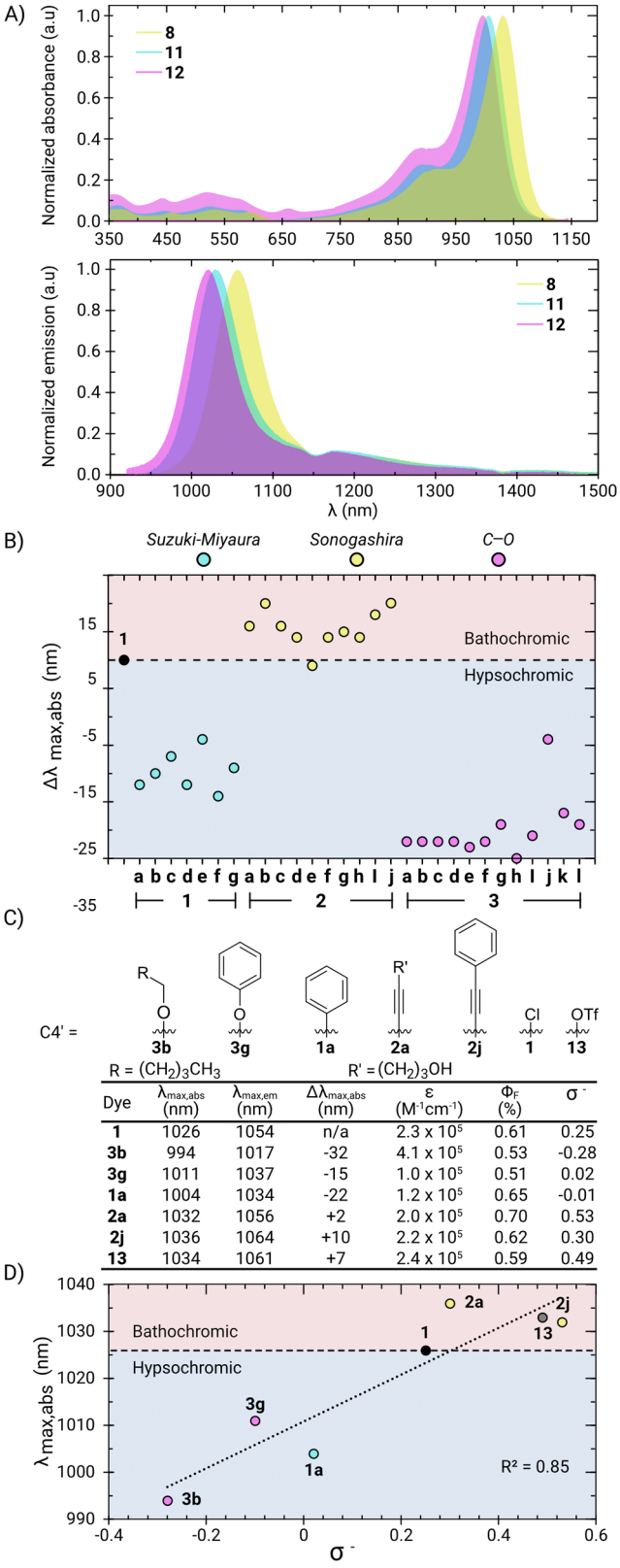

Figure 3. Investigation of $\lambda_{max,abs}$ changes and Hammett analysis of functionalized fluorophores. A) Normalized absorption and emission spectra of functionalized **Flav7** derivatives **8**, **11**, **12** taken in DCM. B) Change in $\lambda_{max,abs}$ of C4′ position modified fluorophores in reference to **Flav7**. C) Structure and photophysical characterization of fluorophores. D) Hammett analysis relating $\lambda_{max,abs}$ and σ^- of functionalized **Flav7** derivatives presented in (C).

and etherification results in the largest hypochromic shift of 30 nm ± 5 nm. One notable exception is the C4′-phenol fluorophore (**3g**), where the hypsochromic shift decreases to 14 nm. We characterized the Φ_F and absorption coefficient at $\lambda_{max,abs}$ (ε_{max}) of each fluorophore and found these metrics to be adequately maintained across the C4′ position functionalized fluorophores with an average Φ_F = 0.58% and ε_{max} = 220,000 M^{-1} cm^{-1} (Figure 3C).

We further analyzed these changes in $\Delta\lambda_{max,abs}$ in relation to the electronic contribution at the C4′ position using linear free energy relationships (LFER). Previous work in the group has established that Hammett plots are valuable for predicting $\lambda_{max,abs}$ changes upon heterocycle modification.[44] Thus, we looked to perform a similar analysis and determine whether we could correlate Hammett parameters and $\lambda_{max,abs}$ in relation to the structural changes at the C4′ position. We selected five of our new fluorophores with published Hammett parameters (or of the closest matching structure, see Figure S7A) and compared these to **Flav7**.[45] To expand the range of Hammett values, we also prepared and characterized fluorophore **13** containing a highly electron withdrawing triflate substituent at the C4′ position. Correlating traditional Hammett parameters with $\lambda_{max,abs}$ showed a modest linear relationship with σ_p (R^2 = 0.69) while σ_m displayed no relationship (R^2 = 0.33, Figure S7B,C). These results suggest that increasing electron donating character at the C4′ position increases the hypsochromic shift, while electron withdrawing groups result in bathochromic shifts. When we compared $\lambda_{max,abs}$ against σ^+ and σ^-, which quantify electron donation via resonance rather than inductive effects, we noticed a stronger correlation with σ^- (R^2 = 0.85) compared to σ^+ (R^2 = 0.66). The linear relationship with σ^- indicates that there may be direct resonance effects at the C4′ position (Figures 3D and S7D).

These results are consistent with electronic effects of heterocycle modification,[44] and support the explanation of the decreased $\Delta\lambda_{max,abs}$ observed with phenol compared to the other C−O-alkyl derivatives. No Hammett parameters gave good correlations when looking at Φ_F and ε_{max}, consistent with our previous analyses of flavylium fluorophores.[44] Overall, our methods to functionalize the C4′ position provide an avenue to modulate the photophysical properties of the fluorophores while simultaneously imparting desirable functionalities.

Fine-Tuning Photophysical Properties for Multiplexed Imaging via C4′ Position Modification

We then applied our newfound understanding of electronic modulation at the C4′ position with existing knowledge regarding heterocycle effects on $\lambda_{max,abs}$ to arrive at three functional fluorophores with optimal properties for excitation-matched multiplexed imaging (Figure 4). Excitation-matched multiplexed imaging is the preferred approach to multicolor imaging in the shortwave infrared region as it allows the brightness of the fluorophores to be maximized by exciting at $\lambda_{max,abs}$.[23,44] We have previously demonstrated excitation-based multiplexed SWIR imaging with unfunctionalized chromenylium polymethine scaffolds, optimizing for excitation at 890, 974 and 1060 nm by changing the length of the polymethine chain for coarse adjustments, followed by fine-tuning with heterocycle modification.[23,44] Understanding the photophysical consequences of modification at the C4′ position can provide another approach to modulate the $\lambda_{max,abs}$ to match the excitation laser while retaining maximal brightness. This strategy is particularly beneficial as a complementary approach

https://doi.org/10.1021/jacsau.4c01279
JACS Au 2025, 5, 2089−2101

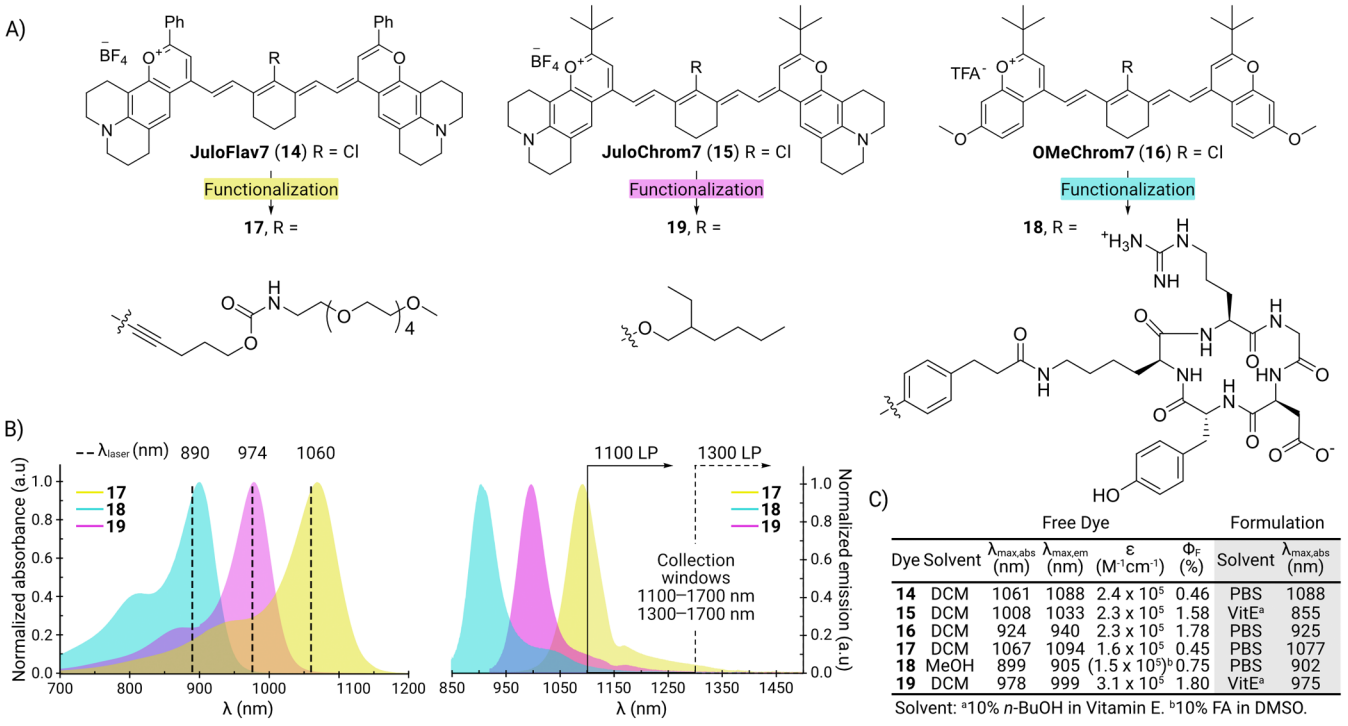

Free Dye | Formulation

Dye	Solvent	$\lambda_{max,abs}$ (nm)	$\lambda_{max,em}$ (nm)	ε ($M^{-1}cm^{-1}$)	Φ_F (%)	Solvent	$\lambda_{max,abs}$ (nm)
14	DCM	1061	1088	2.4 x 10^5	0.46	PBS	1088
15	DCM	1008	1033	2.3 x 10^5	1.58	VitE[a]	855
16	DCM	924	940	2.3 x 10^5	1.78	PBS	925
17	DCM	1067	1094	1.6 x 10^5	0.45	PBS	1077
18	MeOH	899	905	(1.5 x 10^5)[b]	0.75	PBS	902
19	DCM	978	999	3.1 x 10^5	1.80	VitE[a]	975

Solvent: [a]10% *n*-BuOH in Vitamin E. [b]10% FA in DMSO.

Figure 4. Application of the C4′ position coupling methods with different heterocyclic scaffolds affords excitation-matched, functionalized fluorophores. A) Structure and photophysical properties of parent fluorophore scaffold and the final functionalized probes **17**−**19**. B) Normalized absorption and emission spectra of **17**, **19** taken in DCM, and **18** taken in MeOH. C) Table of photophysical properties of free (in DCM or MeOH) and formulated fluorophores (Micelles in PBS; dye dissolved in 10% *n*-BuOH in VitE).

to heterocycle modification. The Hammett analyses suggest that we can predictably fine-tune the $\lambda_{max,abs}$ of a fluorophore and can be used as a guiding metric for the type of transformation that must be imparted at the C4′ position to reach the nearest laser line.

Ultimately, our goal was to employ functional C4′-modified dyes together in an excitation-multiplexed imaging experiment. This goal required combining our knowledge of the λ_{max} changes imparted by C4′ position functionalization with those of heterocycle modification, such that the final fluorophores' $\lambda_{max,abs}$ are spectrally separated and well-matched to commercial excitation laser lines. For 1060 nm excitation, we chose to functionalize **JuloFlav7**, (**14**, $\lambda_{max,abs}$ = 1061 nm, Φ_F = 0.46%), via Sonogashira coupling to minimally perturb its laser-matched $\lambda_{max,abs}$. **JuloChrom7** (**15**, $\lambda_{max,abs}$ = 1008, Φ_F = 1.58%) was selected for 974 nm excitation, expecting a 30 nm hypsochromic shift from etherification at the C4′ position. To achieve an appropriate heptamethine dye for 890 nm excitation, we combined two known heterocycle modification strategies−2-position modification replacing the phenyl group with a *tert*-butyl group (Chrom dyes) and the replacement of the 7-position dimethylamino group with a methoxy group. These modifications resulted in a new fluorophore, **OMeChrom7**, (**16**, $\lambda_{max,abs}$ = 924 nm, Φ_F = 1.60%). We predicted that a 20 nm hypsochromic shift from applying Suzuki-Miyaura coupling to **OMeChrom7** would align the $\lambda_{max,abs}$ near the 890 nm laser line.

The chemistries developed for **Flav7** (Scheme 1 and Scheme 2) were readily translated to these chromenylium scaffolds, and we obtained **JuloFlav7** functionalized with an oligoethylene glycol chain for decreased aggregation in micelle formulations (1060 nm laser, **17**), **OMeChrom7** functionalized with a cRGD moiety for targeting $\alpha_v\beta_{III}$ receptors (890 nm laser, **18**), and **JuloChrom7** functionalized with an ethyl-hexyl group for delivery in oil medium (974 nm laser, **19**) (Figure 4A,B, Schemes S1−S3). Gratifyingly, all fluorophores excellently matched the excitation lasers with $\lambda_{max\ abs,}$ = 899, 977 and 1067 nm, and maintained good quantum yields (>0.40%) and excellent absorption coefficients (>1 × 10^5 M^{-1} cm^{-1}) for the SWIR region. Thus, the functionalization methods developed herein have paved the way for excitation-matched multiplexed imaging in vivo.

Application of Functionalized Fluorophores in Multiplexed In Vivo SWIR Imaging

With the three functionalized, laser-matched fluorophores in hand, we first evaluated their performance with single-color in vivo SWIR imaging in mice. As SWIR heptamethine fluorophores are characteristically hydrophobic, encapsulation in micelle nanocarriers is a common strategy to introduce these dyes to the aqueous biological environment. In principle, micelle nanocarriers are composed of an amphiphilic, biocompatible polymer, and act to sequester fluorophores to a local hydrophobic interior. This leaves the hydrophilic exterior available to interact with the surrounding environment. Hence, the biodistribution of the fluorophore should reasonably be dictated by the identity of the hydrophilic polymer. To test this hypothesis, we previously studied the biodistribution of four chromenylium fluorophores (**Chrom5**, **JuloChrom5**, **Chrom7**, and **JuloFlav7**) encapsulated in identical micelle formulations in mice over 2 days. Surprisingly, we observed distinct localization differences over time, indicating that the fluorophores may be leaching from micelle formulations.[46] Thus, we reason that structural modifications on the C4′ position of similar fluorophores herein will impact the biodistribution upon intravenous (*i.v.*) injection. After

https://doi.org/10.1021/jacsau.4c01279
JACS Au 2025, 5, 2089−2101

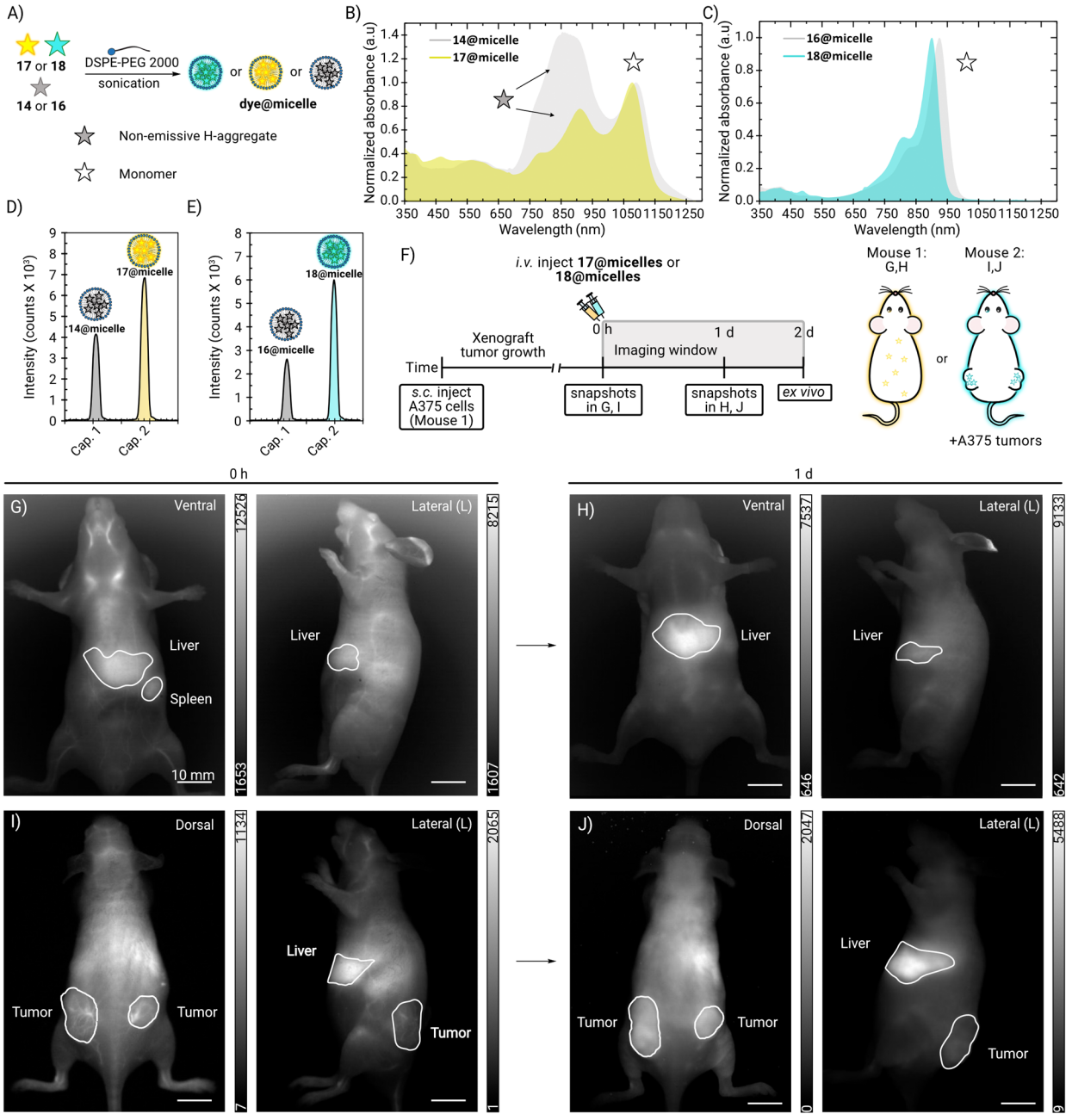

Figure 5. In vivo imaging of **17** and **18** injected via micelle delivery vehicles. A) Scheme of micelle formulation. B,C). Absorbance spectra of **17@micelles** or **18@micelles** in PBS. D,E) Brightness comparison of capillaries with either **17@micelles** or **18@micelles** in PBS. F) Imaging parameters and timeline of injection (not to scale). G,H) SWIR fluorescence images of **17@micelles** (40 μM, 200 μL, 1060 nm excitation, 160 mW cm^{-2}) at t = 0 h, 1 ms ET and t = 1 d, 1 ms ET. I,J) **18@micelles** (39 μM, 200 μL, 890 nm excitation, 135 mW cm^{-2}) at t = 0 min, 5 ms ET and t = 24 h, 3 ms ET. All SWIR fluorescence images were recorded via an InGaAs camera equipped with a 1100 nm LP filter. Scale bar = 10 mm.

demonstrating that functionalized fluorophores encapsulated in micelles were shown to be reasonably stable over 24 h in PBS at physiological temperature (37 °C, Figure S8), we prepared micelle formulations of the PEG and cRGD modified fluorophores, **17** and **18** (respectively) with a PEG-based phospholipid surfactant (Scheme S4). These micelle formulations (**17@micelles** and **18@micelles**) and their unfunctionalized counterparts (**14@micelles** and **16@micelles**) were all ∼9−14 nm in size, as measured by dynamic light scattering (Figures 5A and S9−S11). Analysis of the absorption profile of the **Julo7**-derived scaffolds (**14** and **17**) indicates that the C4′ position modification was beneficial, as the broad signal at ∼800 nm corresponding to nonemissive H-aggregate is decreased (Figure 5B). Conversely, the **OMeChrom7**-derived scaffold (**16** and **18**) displayed monomer character for both the functionalized and parent dyes (Figure 5C), representing our best micelle-encapsulated dyes to date. Comparing SWIR brightness via capillary imaging with an InGaAs camera, **17@micelles** demonstrated a modest 1.8-fold increase in brightness compared to **14@micelles**. We attribute this change to reduced aggregation in **17@micelles** which may arise from the amphiphilic nature and added steric bulk of the functionalized fluorophore. (Figure 5D). Notably, **18@micelles** have a 2.3-fold brightness increase over **16@**

https://doi.org/10.1021/jacsau.4c01279
JACS Au 2025, 5, 2089−2101

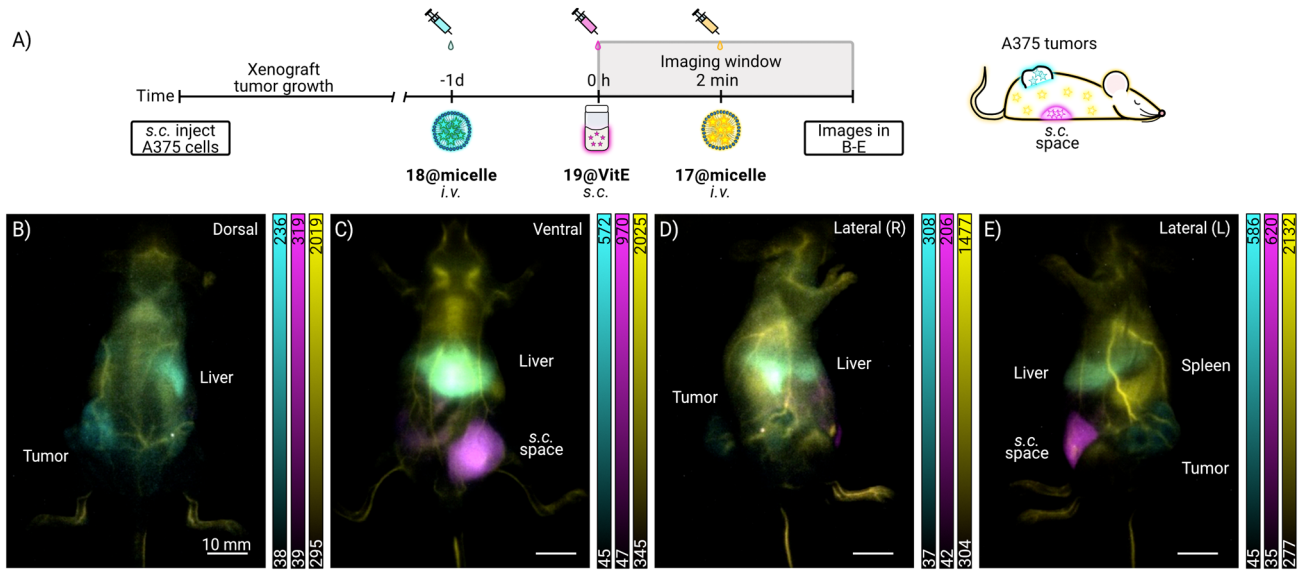

Figure 6. Excitation-multiplexed imaging in xenograft mice. A) Imaging parameters and timeline of injection (not to scale) of **17@micelles** (yellow, 140 μM, 200 μL, 1060 nm excitation, 160 mW cm^{-2}, 6 ms ET), **18@micelles** (cyan, 110 μM, 200 μL, 890 nm excitation, 135 mW cm^{-2}, 2 ms ET), **19@VitE** (magenta, 30 μM, 300 μL, 974 nm excitation, 160 mW cm^{-2}, 20 ms ET). B,C) Merged images of three-color excitation-multiplexed imaging of the (B) dorsal, (C) ventral, (D) lateral, right, and (E) lateral, left sides of the animal. All SWIR fluorescence images were recorded via an InGaAs camera equipped with a 1300 nm LP filter. Scale bars = 10 mm. See Figures S15 and S16 for single channel images and replicate images.

micelles (Figure 5E). This change is likely due to a combination of the $\lambda_{max,abs}$ more closely matching the 890 nm excitation laser, and reduced H-aggregation from steric hindrance of the peptide installed at the C4′ position.

After confirming the photophysical advantage of the functionalized probes, we assessed the in vivo performance of **17@micelles** through *i.v.* injection in mice with excitation at 1060 nm and fluorescence detection via InGaAs camera with a 1100 nm long pass filter to collect photons from 1100 to 1700 nm (Figure 5F). Similar to our previous imaging endeavors with **14@micelles,**[23,44] the vasculature of the mouse was illuminated upon injection, followed by accumulation in the liver, which is a common biodistribution site of fluorophores (Figure 5G). Over the span of 1 day, the fluorophore's blood circulation ceased and fluorescence signal was mostly sustained in the liver (Figure 5H). Two days postinjection, ex vivo organ analysis confirmed strong fluorescence signal in the liver, as well as additional signal throughout other major organs (spleen, kidneys, intestines, stomach, heart, and lungs, Figure S12).

As fluorophore **18** was designed to have affinity for $\alpha_V\beta_{III}$-positive tumors, we also performed a tumor accumulation study of **18@micelles** (49 μM, 200 μL) in mice bearing subcutaneous xenograft tumors (derived from A375 cells) on each hind flank. Upon *i.v.* injection, we quickly observed fluorescence in the vasculature, liver, and spleen (Figure 5H). Notably, the increased level of vascularization around the tumor was observed in great detail. Over time, accumulation within the tumors increased, as evident in the dorsal and lateral views after 1 day postinjection. The ratio of signal intensity between the tumors and other organs of the mouse was quantified to corroborate the accumulation of **18@micelles** in the xenograft tumors. The increasing ratio of signal in the tumors suggests some preferential accumulation to the tumor sites (Figures 5I and S13). Accumulation in the liver is also observed. The micelle encapsulation complicates the targeting mechanism and both passive and active targeting likely play a role. Future work to remove the need for micelle delivery will enhance xenograft imaging experiments.

To showcase the utility of probes **17**, **18**, and **19** in concert, we capitalized on their spectral separation and differential biodistributions for three-color excitation-multiplexed SWIR imaging (Figure 6A). First, **18@micelles** were injected *i.v.* and accumulation in xenograft tumors increased over 1 day, as seen with the prior single-color imaging. At this time, **19@VitE**, with added lipophilicity for solubilization in Vitamin E (α-tocopherol, an essential fat-soluble antioxidant, Figure S14), was administered subcutaneously (*s.c.*), for slow, systemic absorption. A few minutes after, **17@micelles** were injected *i.v.* to illuminate the vasculature of the animal and three-color imaging was performed with video frame rates. Merging individual excitation channels to produce multicolor still images, the dorsal view nicely shows **18@micelles** accumulation within hind flank xenograft tumors (cyan), contrasted by vasculature illumination preceding the **17@micelles** injection (yellow, Figures 6B, S15, and S16). Meanwhile, **19@VitE** was strongly visualized in the subcutaneous space from the ventral and lateral views, which is similarly contrasted by the surrounding **17@micelles**, as well as the spleen (Figure 6C,E). We note that both **17@micelles** and **18@micelles** clear through the liver and became more localized to those sites within a few minutes postinjection (Figure 6C–E).

Overall, three-color excitation-multiplexed imaging with these C4′-functionalized dyes has expanded our ability to noninvasively visualize biology in real-time. For cRGD-modified dye **18**, having increased affinity to diseased sites is of paramount interest to the medical community, as this can help surgeons selectively identify and remove diseased tissue with increased sensitivity. While the targeting property of **18@micelles** has room for improvement, the preference for the target site while boosting the desirable photophysical properties of the core fluorophore in the SWIR region is a notable

https://doi.org/10.1021/jacsau.4c01279
JACS Au 2025, 5, 2089−2101

advance. Additionally, the lipophilic nature of dye **19** has allowed for delivery in an underutilized biologically relevant medium (Vitamin E). Injected *s.c.*, **19@VitE** promotes slow absorption and could enable tracking of its antioxidant and/or immune activity in the body. Finally, the oligoethylene glycol modified dye, **17**, boasts substantially improved brightness in micelle delivery vehicles, allowing less dye to be injected and/or faster imaging acquisition. Here, **17@micelles** also provided increased contrast for both the tumor localization of **18@micelles** and *s.c.* absorption of **19@VitE**, providing a clearer picture of murine cancer models as well as xenobiotic substance absorption. Collectively, these examples illustrate the power and potential of C4′ position modifications for improving in vivo SWIR imaging.

CONCLUSIONS

We present a one step, Pd-catalyzed C4′ position functionalization of SWIR heptamethine flavylium and chromenylium fluorophores utilizing three distinct classes of coupling partners. One common palladium catalyst, $Pd(PPh_3)_4$, was effective at invoking Suzuki-Miyaura, Sonogashira, as well as a new C−O-alkyl transformation to the **Flav7** scaffold. The substrate scope presented provides functional handles by which these fluorophores can be further derivatized, facilitating the conjugation of lipophilic, aggregation minimizing, or targeting moieties to SWIR-emissive fluorophores. The photophysical properties of the C−O-alkyl, $C-C_{Ar}$, and $C-C_{sp}$ linkages at the C4′ position were investigated with Hammett analysis to provide a predictive metric for $\lambda_{max,abs}$ modulation, revealing that $C-C_{Ar}$ and C−O-alkyl transformations at the C4′ position hypsochromatically shifted the $\lambda_{max,abs}$ by a maximum of 30 nm while $C-C_{sp}$ provided on average a 5 nm bathochromic shift. These predictive metrics were applied to two different established SWIR-emissive chromophores, **JuloChrom7** and **JuloFlav7**, and a newly developed probe, **OMeChrom7**, resulting in functionalized fluorophores excellently matching commercial laser lines (890, 974, and 1060 nm). The functionalities imparted to these fluorophores demonstrate the ability to imbue existing fluorophores with new solubility properties (**19**), enhanced brightness in micelles (**17**, **18**), and/or affinity probes (**18**). These fluorophores proved to be excellent contrast agents for in vivo imaging, outperforming their unfunctionalized counterparts, and were applied synchronously to image the vasculature, *s.c.* space, and xenograft tumors in live mice. This report demonstrates the power of functionalizing SWIR scaffolds at the C4′ position to transform the utility of existing heptamethine fluorophores and translate it to new applications for in vivo imaging in the SWIR region.

METHODS

Materials

All chemical reagents were purchased from commercial suppliers and used without further purification. Anhydrous, deoxygenated solvents were dispensed from a Grubb's-type Phoenix Solvent Drying System constructed by the late JC Meyer or dried over molecular sieves.

Synthetic Procedures

General cross coupling procedure to yield compounds **1a−1g** and **2a−2j**: **Flav7** (0.026 mmol, 1.0 equiv), K_3PO_4 (0.13 mmol, 5.0 equiv), $Pd(PPh_3)_4$ (0.0026 mmol, 0.10 equiv), and the appropriate coupling partner (0.13 mmol, 5.0 equiv) were dissolved in 5:1 1,4-dioxane:H_2O (0.60 mL) in a flame-dried air free Schlenk flask under N_2 atmosphere. The solution was freeze-pumped-thawed three times and heated to 90 °C for 24 h. The crude reaction mixture was evaporated, loaded onto silica gel, and purified by column chromatography using a 0.5−15% DCM to EtOH gradient.

General cross coupling procedure to yield compounds **3a−l**: **Flav7** (0.013 mmol, 1.0 equiv), NaOPiv (0.039 mmol, 3.0 equiv), $Pd(PPh_3)_4$ (0.0013 mmol, 0.10 equiv), and the appropriate alcohol coupling partner (0.52 mmol, 40 equiv) were dissolved in 10:1 1,4-dioxane:H_2O (0.30 mL) in a flame-dried microwave vial under N_2 atmosphere. The solution was freeze-pumped-thawed three times and heated for 20 min at 120 °C in a microwave reactor. The crude mixture was evaporated, loaded onto silica gel, and purified by column chromatography using a 0.5−15% DCM to EtOH gradient.

Synthesis of **17**: **JuloFlav7** (0.022 mmol, 1.0 equiv), K_3PO_4 (0.11 mmol, 5.0 equiv), $Pd(PPh_3)_4$ (0.0022 mmol, 0.10 equiv), and pent-4-yn-1-ol (0.12 mmol, 5.0 equiv) were dissolved in 5:1 1,4-dioxane:H_2O (0.60 mL) in a flame-dried air free Schlenk flask under N_2 atmosphere. The solution was freeze-pumped-thawed three times and heated to 90 °C for 24 h. The crude reaction mixture was evaporated, loaded onto silica gel, and purified by column chromatography using a 0.5−15% DCM to EtOH gradient to yield **S5** (0.014 mmol, 62%). Compound **S5** (0.011 mmol, 1.0 equiv), pyridine (0.028 mmol, 3.0 equiv), and 4-nitrobenzoyl chloride (0.028 mmol, 3.0 equiv) were dissolved in DCM (1.0 mL) and stirred at room temperature for 2 h. The crude mixture was evaporated, loaded onto silica gel, and purified by column chromatography using a 0.5 to 15% DCM to EtOH gradient to yield **S6** (0.0091 mmol, 82%). Carbonate **S6** (0.0038 mmol, 1.0 equiv), TEA (0.0038 mmol, 1.0 equiv), and 2,5,8,11,14-pentaoxahexadecan-16-amine (0.0056 mmol 1.5 equiv) were dissolved in DCM (1.0 mL) and stirred at room temperature for 2 h. The crude mixture was evaporated, loaded onto silica gel, and purified by column chromatography using a 0.5−15% DCM to EtOH gradient to yield **17** (0.0028 mmol, 72%).

Synthesis of **18**: **OMeChrom7** (0.014 mmol, 1.0 equiv), K_3PO_4 (0.070 mmol, 5.0 equiv), $Pd(PPh_3)_4$ (0.0014 mmol, 0.10 equiv), and 3-(4-boronophenyl)propanoic acid (0.070 mmol, 5.0 equiv) were dissolved in 5:1 1,4-dioxane:H_2O (0.30 mL) in a flame-dried air free Schlenk flask under N_2 atmosphere. The solution was freeze-pumped-thawed three times and heated to 100 °C for 24 h. The crude mixture was evaporated, loaded onto silica gel, and purified by column chromatography using a 0.5−15% DCM to EtOH gradient to yield **S3** (0.0081 mmol, 18%). Compound **S3** (0.025 mmol, 1.0 equiv), TEA (0.13 mmol, 5.0 equiv), and pentafluorophenyl carbonate (0.13 mmol, 5.0 equiv) were dissolved in DCM (2.5 mL) and stirred at room temperature for 2 h. The crude mixture was evaporated, loaded onto silica gel, and purified by column chromatography using a 0.5 to 15% DCM to EtOH gradient to form **S4** (0.018 mmol, 70%). The activated ester **S4** (0.016 mmol, 1.0 equiv), *N*,*N*-diisopropylethylamine (0.51 mmol, 30 equiv), and cyclo(RGDyK) (0.051 mmol, 3.0 equiv) were dissolved in *N*-methylpyrrolidone (5.0 mL) and stirred for 16 h at room temperature. Afterward, the crude solution was evaporated by a N_2 stream overnight then washed with ether and toluene. The crude product was then recrystallized in a 0.1% TFA-MeCN solution to yield **18** (0.0092 mmol, 57%).

Synthesis of **19**: **JuloChrom7** (0.012 mmol, 1.0 equiv), NaOPiv (0.037 mmol, 3.0 equiv), $Pd(PPh_3)_4$ (1.4 mg, 0.0012 mmol, 0.10 equiv), 2-ethyl hexanol (0.49 mmol, 40 equiv) were dissolved in 10:1 1,4-dioxane:H_2O (0.30 mL) in a flame-dried microwave vial under N_2 atmosphere. The solution was freeze-pumped-thawed three times and heated for 20 min at 120 °C in a microwave reactor. The crude mixture was evaporated, loaded onto silica gel, and purified by column chromatography using a 0.5−15% DCM to EtOH gradient to yield **19** (0.0041 mmol, 33%).

Detailed synthetic procedures for all cross-coupled and functionalized compounds can be found in the Supporting Information.

Photophysical Characterizations

Absorbance spectra were collected on a JASCO V-770 UV-visible/NIR spectrophotometer. Photoluminescence spectra were obtained on a Horiba Instruments PTI QuantaMaster Series fluorometer with InGaAs detector Horiba Edison DSS IGA 020L. Quartz cuvettes (10

https://doi.org/10.1021/jacsau.4c01279
JACS Au 2025, 5, 2089−2101

mm × 10 mm) were used for absorbance and photoluminescence measurements. Absorption coefficients were calculated from serial dilutions of the unknown dye using Hamilton syringes in volumetric glassware. For relative quantum yield calculations, fluorescence spectra of fluorophores were collected with excitation at 800, 840, or 855 nm (defined for each experiment, see "Supplementary Notes") with a 900 nm SP filter (Thorlabs FES 900) and collection from 840-, 880-, or 920−1500 nm. Relative quantum yields were calculated using reference standards **IR-26**[47] or **Chrom7**.[23] All spectra were measured at room temperature with freshly prepared samples. Solvents used for photophysical measurements are reported in the Supporting Information.

LCMS Analysis

Low resolution liquid chromatography mass spectrometry was obtained using a 1260 Infinity II, Agilent 6100 series quadrupole LC/MSD equipped with a Zorbax SB-C18 column (Agilent). Determination of conversion by LCMS was performed with an aliquot of the crude reaction mixtures (approximately 1.0 mg/mL of material). The crude was dissolved in 0.1% TFA MeCN, filtered through Celite then a 0.22 μM filter, and analyzed with a 0.1% FA MeCN:H_2O mobile phase using a 65−95% gradient. Conversion was calculated by integrating the LCMS absorbance signal at 254 nm (using the manual integration function of the OpenLab ChemStation software).

Preparation of Micelle Formulations

General encapsulation procedure: A solution of 18:0 PEG2000 PE (1,2-distearoyl-*sn*-glycero-3-phosphoethanolamine-*N*-[methoxy-(polyethylene glycol)-2000] ammonium salt (Avanti Polar Lipids, 24 mg) dissolved in Milli-Q water (4.0 mL) was added to a separate solution composed of the desired fluorophore (0.20 mg) in DMSO (4.0 mL) in a 50 mL falcon tube. The combined solutions were placed on an ice bath and sonicated for 90 s at 35% amplitude. The solution was then placed on 10 kDa MW cutoff filter (Amicon Ultra-15) and centrifuged (4000 g) for 12 min. 1X PBS (pH = 7.4) or Milli-Q water was added to the solution and concentrated via centrifugation again. This process was repeated three times.

Xenograft Procedures

Cells were purchased from the American Type Culture Collection (ATCC). A375 cells were cultured in complete Dulbecco's Modified Eagle Media (DMEM, Life Technologies, Catalog number: 11995073) supplemented with 10% FBS, 100 mM sodium pyruvate and 1% penicillin-streptomycin at 37 °C under 5% CO_2. Cells were grown to 70−80% confluency, harvested, and washed with PBS three times. For each xenograft implantation, 1.5 × 10^6 cells were suspended in PBS (100 μL) and combined with Matrigel membrane matrix (100 μL) to support cells in vivo. Mice were first anesthetized by inhalation of 2−4% isoflurane. The hind flank skin of the animal was raised, and a 29-gauge needle syringe (VetriJec Insulin Syringe) prefilled with the cell mixture was inserted. The cell mixture was then injected subcutaneously (*s.c.*) and allowed to settle for approximately 30 s before removing the needle. Xenografts were monitored for growth via caliper measurements. Xenograft tumors measured ∼94−440 mm^3 for in vivo imaging experiments.

In Vivo Imaging

Animal imaging experiments were performed according to the University of California, Los Angeles guidelines. The Animal Research Committee approved all protocols (protocol number: ARC-2018-047). Noninvasive, whole mouse imaging was performed with athymic NU/J female mice (6−16 weeks old). Mice were anesthetized by inhalation of 2−4% isoflurane during all imaging procedures. Intravenous (*i.v.*) tail vein injections (200 μL total, at once) were done with a catheter assembled by 29-gauge needle connected through plastic tubing prefilled with isotonic saline solution. The catheter tubing was connected to a 29-gauge needle syringe prefilled with the fluorophore solution of interest. Injections to the subcutaneous (*s.c.*) space (300 μL total, per injection) were performed with a 29-gauge needle syringe filled with the fluorophore solution of interest. In vivo imaging was performed on a custom-built SWIR imaging setup equipped with an InGaAs (Allied Vision Goldeye G-032 Cool TEC2) camera.

■ ASSOCIATED CONTENT

Supporting Information

The Supporting Information is available free of charge at https://pubs.acs.org/doi/10.1021/jacsau.4c01279.

Chart S1, Table S1, Schemes S1−S4, Figures S1−S16, experimental procedures for main text and supplementary figures, experimental data and characterization of all new compounds (PDF)

■ AUTHOR INFORMATION

Corresponding Author

Ellen M. Sletten − *Department of Chemistry and Biochemistry, University of California, California 90095, United States;* orcid.org/0000-0002-0049-7278; Email: sletten@chem.ucla.edu

Authors

Cesar A. Garcia − *Department of Chemistry and Biochemistry, University of California, California 90095, United States*

Emily B. Mobley − *Department of Chemistry and Biochemistry, University of California, California 90095, United States;* orcid.org/0000-0002-4638-1123

Eric Y. Lin − *Department of Chemistry and Biochemistry, University of California, California 90095, United States*

Kyle Bui − *Department of Chemistry and Biochemistry, University of California, California 90095, United States*

Complete contact information is available at: https://pubs.acs.org/10.1021/jacsau.4c01279

Notes

The authors declare no competing financial interest.

■ ACKNOWLEDGMENTS

This material is based upon work supported by the National Science Foundation Graduate Research Fellowship Program under Grant No. DGE-2034835 (C.A.G). Any opinions, findings, and conclusions or recommendations expressed in this material are those of the authors and do not necessarily reflect the views of the National Science Foundation. We also acknowledge National Science Foundation's grant CHE-2204263, the National Institute of Biological Imaging and Bioengineering (1R01EB027172 to E.M.S.) and the Tobacco Related Disease Research Program (T32DT4847 to E.Y.L.). We also extend our gratitude to Dr. Yuh Guo Pan and Charles J. Pederson for fellowships to C.A.G and the UCLA Jonsson Comprehensive Cancer Center for fellowship to E.B.M. Compound characterization data was supported by NIH (S10OF028644) and NSF (CHE-1048804) shared instrumentation grants. Finally, the authors would like to thank Nika Gladkov for designing the cover art submitted with this manuscript.

■ ABBREVIATIONS

cRGD	cyclic peptide RGDyK
DCM	dichloromethane
DMF	dimethylformamide
DMSO	dimethyl sulfoxide

EPR	enhanced permeability and retention
ET	exposure time
FDA	United States Food and Drug Administration
fps	frames per second
h	hour
Het	heterocycle
HOMO	highest occupied molecular orbital
ICG	indocyanine green
i.v.	intravenous
LC-MS	liquid chromatography−mass spectrometry
LP	long-pass (filter)
LUMO	lowest occupied molecular orbital
MeCN	acetonitrile
MeOH	methanol
NaAsc	sodium ascorbate
NaOAc	sodium acetate
NaOPiv	sodium pivalate
NIR	near-infrared
NMP	*N*-methyl pyrrolidone
OA	oxidative addition
PBS	phosphate buffered saline
PFP	pentafluorophenyl
Pyr	pyridine
RT	room temperature
s.c.	subcutaneous
S_NAr	nucleophilic aromatic substitution
SWIR	shortwave infrared
TBAF	tetrabutyl ammonium fluoride
TEA	triethylamine
TFA	trifluoroacetate
THPTA	tris-hydroxypropyltriazolylmethylamine
TMS	trimethylsilane
VitE	vitamin E

REFERENCES

(1) Lavis, L. D.; Raines, R. T. Bright Building Blocks for Chemical Biology. *ACS Chem. Biol.* **2014**, *9*, 855−866.

(2) Frangioni, J. V. In Vivo Near-Infrared Fluorescence Imaging. *Curr. Opin. Chem. Bio.* **2003**, *7*, 626−634.

(3) Li, H.; Kim, Y.; Jung, H.; Hyun, J. Y.; Shin, I. Near-Infrared (NIR) Fluorescence-Emitting Small Organic Molecules for Cancer Imaging and Therapy. *Chem. Soc. Rev.* **2022**, *51*, 8957−9008.

(4) Zhu, S.; Tian, R.; Antaris, A. L.; Chen, X.; Dai, H. Near-Infrared-II Molecular Dyes for Cancer Imaging and Surgery. *Adv. Mater.* **2019**, *31*, No. 1900321.

(5) Pogue, B. W. Perspective Review of What is Needed for Molecular-specific Fluorescence-guided surgery. *J. Biomed. Opt.* **2018**, *23*, No. 100601.

(6) Mahalingam, S. M.; Kularatne, S. A.; Myers, C. H.; Gagare, P.; Norshi, M.; Liu, X.; Singhal, S.; Low, P. S. Evaluation of Novel Tumor-Targeted Near-Infrared Probe for Fluorescence-Guided Surgery of Cancer. *J. Med. Chem.* **2018**, *61*, 9637−9646.

(7) Strekowski, L.; Lipowska, M.; Patonay, G. Facile Derivatizations of Heptamethine Cyanine Dyes. *Synth. Commun.* **1992**, *19*, 2593−2598.

(8) Haque, A.; Faizi, M. S. H.; Rather, J. A.; Khan, M. S. Next Generation NIR Fluorophores for Tumor Imaging and Fluorescence-Guided Surgery: A Review. *Bioorg. Med. Chem.* **2017**, *25*, 2017−2034.

(9) Chen, C.; Tian, R.; Zeng, Y.; Chu, C.; Liu, G. Activatable Fluorescence Probes for "Turn-On" and Ratiometric Biosensing and Bioimaging: From NIR-I to NIR-II. *Bioconjugate. Chem.* **2020**, *31*, 276−292.

(10) Lin, C. M.; Usama, S. M.; Burgess, K. Site−Specific Labeling of Proteins with Near−IR Heptamethine Cyanine Dyes. *Molecules.* **2018**, *23*, 2900.

(11) Strekowski, L.; Lipowska, M.; Patonay, G. Substitution Reactions of a Nucleofugal Group in Heptamethine Cyanine Dyes. Synthesis of an Isothiocyanato Derivative for Labeling of Proteins with a Near-Infrared Chromophore. *J. Org. Chem.* **1992**, *57*, 4578−4580.

(12) Zhao, X.; Zhang, F.; Lei, Z. The Pursuit of Polymethine Fluorophores with NIR-II Emission and High Brightness for in vivo Applications. *Chem. Sci.* **2022**, *13*, 11280−11293.

(13) Li, Y.; Zhou, Y.; Yue, X.; Dai, Z. Cyanine Conjugates in Cancer Theranostics. *Bioact. Mater.* **2021**, *6*, 794−809.

(14) Choi, H. S.; Nasr, K.; Alyabyev, S.; Feith, D.; Lee, J. H.; Kim, S. H.; Ashitate, Y.; Hyun, H.; Patonay, G.; Strekowski, L.; Henary, M.; Frangioni, J. V. Synthesis and In Vivo Fate of Zwitterionic Near-Infrared Fluorophores. *Angew. Chem., Int. Ed.* **2011**, *50*, 6258−6263.

(15) Hyun, H.; Owens, E. A.; Narayana, L.; Wada, H.; Gravier, J.; Bao, K.; Frangioni, J. V.; Choi, H. S.; Henary, M. Central C−C Bonding Increases Optical and Chemical Stability of NIR Fluorophores. *RSC Adv.* **2014**, *4*, 58762−58768.

(16) Nani, R. R.; Shaum, J. B.; Gorka, A. P.; Schnermann, M. J. Electrophile-Integrating Smiles Rearrangement Provides Previously Inaccessible C4′-O-Alkyl Heptamethine Cyanine Fluorophores. *Org. Lett.* **2015**, *17*, 302−305.

(17) König, S. G.; Krämer, R. Accessing Structurally Diverse Near-Infrared Cyanine Dyes for Folate Receptor-Targeted Cancer Cell Staining. *Chem.—Eur. J.* **2017**, *23*, 9306−9312.

(18) Lee, H.; Mason, J. C.; Achilefu, S. Heptamethine Cyanine Dyes with a Robust C−C Bond at the Central Position of the Chromophore. *J. Org. Chem.* **2006**, *71*, 7862−7865.

(19) Thimsen, E.; Sadtler, B.; Berezin, M. Y. Shortwave-infrared (SWIR) Emitters for Biological Imaging: A Review of Challenges and Opportunities. *Nanophotonics.* **2017**, *6*, 1043−1054.

(20) Wong, K. C. Y.; Sletten, E. M. Extending Optical Chemical Tools and Technologies to Mice by Shifting to the Shortwave Infrared Region. *Curr. Opin. Chem. Biol.* **2022**, *68*, No. 102131.

(21) Ou, Y. F.; Ren, T. B.; Yuan, L.; Zhang, X. B. Molecular Design of NIR-II Polymethine Fluorophores for Bioimaging and Biosensing. *Chem. Biol. Imaging.* **2023**, *1*, 220−233.

(22) Lei, Z.; Zhang, F. A. Molecular Engineering of NIR-II Fluorophores for Improved Biomedical Detection. *Angew. Chem., Int. Ed.* **2021**, *60*, 16294−16308.

(23) Cosco, E. D.; Arús, B. A.; Spearman, A. L.; et al. Bright Chromenylium Polymethine Dyes Enable Fast, Four-color in vivo Imaging with Shortwave Infrared Detection. *J. Am. Chem. Soc.* **2021**, *143*, 6836−6846.

(24) Arús, B. A.; Cosco, E. D.; Yiu, J.; Balba, I.; Bischof, T. S.; Sletten, E. M.; Bruns, O. T. Shortwave Infrared Fluorescence Imaging of Peripheral Organs in Awake and Freely Moving Mice. *Front. Neurosci.* **2023**, *17*, No. 1135494.

(25) Wang, Y.; Ogasahara, K.; Tomihama, D.; Mysliborski, R.; Ishida, M.; Hong, Y.; Notsuka, Y.; Yamaoka, Y.; Murayama, T.; Muranaka, A.; Uchiyama, M.; Mori, S.; Yasutake, Y.; Fukatsu, S.; Kim, D.; Furuta, H. Near-Infrared-III-Absorbing and-Emitting Dyes: Energy-Gap Engineering of Expanded Porphyrinoids via Metallation. *Angew. Chem.* **2020**, *37*, 16295−16300.

(26) Fabian, J. Symmetry-lowering Distortion of Near-infrared Polymethine Dyes—A Study by First-principles Methods. *J. Mol. Struct.: THEOCHEM* **2006**, *766*, 49−60.

(27) Sajid, H.; Ayub, K.; Arshad, M.; Mahmood, T. Highly Selective Acridinium based Cyanine Dyes for the Detection of DNA Base Pairs (Adenine, Cytosine, Guanine and Thymine). *Comput. Theor. Chem.* **2019**, *1163*, No. 112509.

(28) Medeiros, N. G.; Braga, C. A.; Câmara, V. S.; Duarte, R. C.; Rodembusch, F. S. Near-Infrared Fluorophores Based on Heptamethine Cyanine Dyes: From Their Synthesis and Photophysical Properties to Recent Optical Sensing and Bioimaging Applications. *Asian J. Org. Chem.* **2022**, *11*, No. e202200095.

(29) Guo, L.; Yang, M.; Dong, B.; Lewman, S.; Van Horn, A.; Jia, S. Engineering Central Substitutions in Heptamethine Dyes for Improved Fluorophore Performance. *JACS Au* **2024**, *4*, 3007−3017.

https://doi.org/10.1021/jacsau.4c01279
JACS Au 2025, 5, 2089−2101

(30) Zhang, H.; Ruiz-Castillo, P.; Buchwald, S. L. Palladium-Catalyzed C-O Cross-Coupling of Primary Alcohols. *Org. Lett.* **2018**, *20*, 1580−1583.
(31) Jia, S.; Lin, E. Y.; Mobley, E. B.; Lim, I.; Guo, L.; Kallepu, S.; Low, P. S.; Sletten, E. M. Water-soluble Chromenylium Dyes for Shortwave Infrared Imaging in Mice. *Chem.* **2023**, *9*, 3648−3665.
(32) Fuhrmann, E.; Talbiersky, J. Synthesis of Alkyl Aryl Ethers by Catalytic Williamson Ether Synthesis with Weak Alkylation Agents. *Org. Process Res. Dev.* **2005**, *9*, 206−211.
(33) Lin, H.; Sun, D. Recent Synthetic Developments and Applications of the Ullmann Reaction. a Review. *Org. Prep. Proced. Int.* **2013**, *45*, 341−394.
(34) Swamy, K. C. K.; Kumar, N. N. B.; Balaraman, E.; Kumar, K. V. P. P. Mitsunobu and Related Reactions: Advances and Applications. *Chem. Rev.* **2009**, *109*, 2551−2651.
(35) Fletcher, S. The Mitsunobu Reaction in the 21 St Century *Org. Chem. Front.* **2015**, *2*, 739.
(36) Davydenko, I.; Barlow, S.; Sharma, R.; Benis, S.; Simon, J.; Allen, T. G.; Cooper, M. W.; Khrustalev, V.; Jucov, E. V.; et al. Facile Incorporation of Pd (PPh_3) 2Hal Substituents into Polymethines, Merocyanines, and Perylene Diimides as a Means of Suppressing Intermolecular Interactions. *J. Am. Chem. Soc.* **2016**, *138*, 10112−10115.
(37) Rojas, A. J.; Wolfe, J. M.; Dhanjee, H. H.; Buslov, I.; Truex, N. L.; Liu, R. Y.; Massefski, W.; Pentelute, B. L.; Buchwald, S. L. Palladium-Peptide Oxidative Addition Complexes for Bioconjugation. *Chem. Sci.* **2022**, *13*, 11891−11895.
(38) Liu, S. Radiolabeled Multimeric Cyclic RGD Peptides as Integrin $\alpha_v\beta_3$ Targeted Radiotracers for Tumor Imaging. *Mol. Pharmaceutics* **2006**, *3*, 472−487.
(39) Ye, Y.; Bloch, S.; Xu, B.; Achilefu, S. Design, Synthesis, and Evaluation of near Infrared Fluorescent Multimeric RGD Peptides for Targeting Tumors. *J. Med. Chem.* **2006**, *49*, 2268−2275.
(40) Zhao, M.; Ding, J.; Mao, Q.; Zhang, Y.; Gao, Y.; Ye, S.; Qin, H.; Shi, H. A Novel α v β 3 Integrin-Targeted NIR-II Nanoprobe for Multimodal Imaging-Guided Photothermal Therapy of Tumors in Vivo. *Nanoscale* **2020**, *12*, 6953−6958.
(41) Ding, B.; Xiao, Y.; Zhou, H.; Zhang, X.; Qu, C.; Xu, F.; Deng, Z.; Cheng, Z.; Hong, X. Polymethine Thiopyrylium Fluorophores with Absorption beyond 1000 Nm for Biological Imaging in the Second Near-Infrared Subwindow. *J. Med. Chem.* **2019**, *62*, 2049−2059.
(42) de Valk, K. S.; Deken, M. M.; Handgraaf, H. J. M.; Bhairosingh, S. S.; Bijlstra, O. D.; van Esdonk, M. J.; Terwisscha van Scheltinga, A. G. T.; Valentijn, A. R. P. M.; March, T. L.; Vuijk, J.; Peeters, K. C. M. J.; Holman, F. A.; Hilling, D. E.; Mieog, J. S. D.; Frangioni, J. V.; Burggraaf, J.; Vahrmeijer, A. L.; et al. First-in-Human Assessment of CRGD-ZW800-1, a Zwitterionic, Integrin-Targeted, Near-Infrared Fluorescent Peptide in Colon Carcinoma. *Clin. Cancer Res.* **2020**, *26*, 3990−3998.
(43) Gamage, R. S.; Li, D. H.; Schreiber, C. L.; Smith, B. D. Comparison of CRGDfK Peptide Probes with Appended Shielded Heptamethine Cyanine Dye (S775z) for near Infrared Fluorescence Imaging of Cancer. *ACS Omega* **2021**, *6*, 30130−30139.
(44) Cosco, E. D.; Arús, B. A.; Spearman, A. L.; et al. Shortwave infrared polymethine fluorophores matched to excitation lasers enable non-invasive, multicolour in vivo imaging in real time. *Nat. Chem.* **2020**, *12*, 1123−1130.
(45) Hansch, C.; Leo, A.; Taft, R. W. A Survey of Hammett Substituent Constants and Resonance and Field Parameters. *Chem. Rev.* **1991**, *91*, 165−195.
(46) Lim, I. Fluorous-soluble chromophores for imaging and therapeutics in vivo **2022**, *UCLA*, Doctoral dissertation.
(47) Semonin, O. E.; Johnson, J. C.; Luther, J. M.; Midgett, A. G.; Nozik, A. J.; Beard, M. C. Absolute Photoluminescence Quantum Yields of IR-26 Dye, PbS, and PbSe Quantum Dots. *J. Phys. Chem. Lett.* **2010**, *1*, 2445−2450.

https://doi.org/10.1021/jacsau.4c01279
JACS Au 2025, 5, 2089−2101